Pure Appl. Geophys.
© 2020 Springer Nature Switzerland AG
https://doi.org/10.1007/s00024-020-02528-7

Pure and Applied Geophysics

Analytical Model for Tsunami Propagation Including Source Kinematics

Mauricio Fuentes,[1] Francisco Uribe,[1] Sebastián Riquelme,[2] and Jaime Campos[1]

Abstract—There are only a few analytical 2+1D models for tsunami propagation, most of which treat tsunami generation from a static deformation field isolated from the kinematics of the rupture. This work examines the behavior of tsunami propagation in a simple setup including a source time function which accounts for a time description of the rupture process on the tsunami source. An analytical solution is derived in the wavenumber domain, which is quickly inverted to space with the fast Fourier transform. The solution is obtained in closed form in the 1+1D case. The inclusion of temporal parameters of the source such as rise time and rupture velocity reveals a specific domain of very slow earthquakes that enhance tsunami amplitudes and produce non-negligible shifts in arrival times. The results confirm that amplification occurs when the rupture velocity matches the long-wave tsunami speed, and the static approximation corresponds to a limit case for (relatively) fast ruptures.

Keywords: Tsunami, seismology, analytical model.

1. Introduction

In most cases, tectonic tsunamis are modeled as shallow water phenomena excited by large subduction earthquakes. These earthquakes radiate seismic waves from a source described by a rupture front and a dislocation vector at each point of the source. This deformation can last several seconds, but is normally assumed to be instantaneous when compared with tsunami time scales. This was first observed by Kajiura (1970), who constructed an analytical model that included a rise time but assumed an infinite rupture velocity. From that study, it was concluded that the instantaneous approach is suitable because of the minor effect that standard values of rise time have on tsunami generation.

A pioneering work by Novikova and Ostrovsky (1979) questioned the static approach and studied the physics of the process of wave generation by a propagating deformation of the sea floor. The energy radiation was calculated, and an optimal situation was found for a synchronous moving floor. Later, Novikova and Ostrovsky (1982) examined cases where a nonlinear hydroacoustic mechanism could contribute to tsunami waves.

Schmedes et al. (2010) computed 315 dynamic strike-slip rupture scenarios to produce probability density functions of several kinematic parameters. The most likely values for rise time are $\sim 2-4$ s and for rupture velocity $\sim 2.0-2.7$ km/s. The computation was performed in a half space with a layer over it, spanning S-wave velocities from 2.0 to 3.0 km/s, with a fixed shape of the source time function. This study also proposes a relation between rise time (via peak slip rate) and rupture velocity.

A far-field approximation was obtained by Yamashita and Sato (1974) to study the effect of focal parameters. In particular, the dip angle, fault length and focal depth are important factors with regard to tsunami amplitudes because of the initial wave generation, but kinematic parameters were also analyzed, where shorter rise times contribute more to the amplitudes. There are also preferred directions where rupture velocity intensifies the spectral amplitudes. However, the authors fixed the rupture velocity at 3 km/s because the last four largest earthquakes near Japan were of this order.

Todorovska and Trifunac (2001) used the linear tsunami potential theory to construct a 2+1D analytical model. The forcing term was modeled as a uniform hump with a constant rupture speed front

Electronic supplementary material The online version of this article (https://doi.org/10.1007/s00024-020-02528-7) contains supplementary material, which is available to authorized users.

[1] Department of Geophysics, University of Chile, Santiago, Chile.

[2] National Seismological Center, University of Chile, Santiago, Chile.

Published online: 23 June 2020

propagating unilaterally. However, they did not include a rise time in their model (instantaneous rise time) and observed amplification in the waves associated with constructive interference due to coupling of the rupture and the tsunami wave propagation. The same year, Ward (2001) provided an analytical study of tsunami excitation from simple slides, obtaining the same solution as Todorovska and Trifunac (2001) but in a different context. Also, Ward (2001) assumed linearity to reproduce complex slides via Green's function summations.

Saito (2013) also used the linear tsunami potential theory to analyze the velocity field when the initial condition is generated with a finite rise time. The study claims to obtain an analytical solution for an arbitrary source time function, but the solution is only semi-analytical, since it depends on the numerical inverse Fourier transform, and the source time function does not consider rupture propagation. Nevertheless, the solution allows one to quantify the weights of static and dynamic pressures, which is fundamental for fast source inversion methods that use ocean-bottom stations.

Le Gal et al. (2017) used the model of Todorovska and Trifunac (2001) in a 1+1D version modified to include a half-sine rise time function. Results from their study confirmed the findings about resonance when rupture velocity equals the tsunami propagation velocity, but the effect is attenuated for long rise times. The obtained linear solution explains as much as the fully nonlinear shallow water theory. Thus, this work was extended to 2+1D to model the 1947 Gisborne and 2011 Tohoku-Oki tsunamis (Le Gal et al. 2018).

The inclusion of a sloping beach geometry to study the 1+1D linear run-up for a kinematic seismic source was examined by Fuentes et al. (2018). The authors observed similar features in wave amplification. The run-up also showed amplifications up to five times relative to the static case when there was a coupling between the tsunami wave propagation and the source rupture velocity.

The case of tsunami generation due to a strip in a finite-depth ocean was investigated by Carrier and Yeh (2005), and an analytical solution was obtained for an initial value problem. The main characteristics of a large source with a finite aspect ratio were discussed. The solution confirms a degradation rate $O\left(\frac{1}{\sqrt{r}}\right)$. Further simplifications of the formulation were addressed by Kânoğlu et al. (2013), overcoming the problems that arise when complete elliptical integral functions are used. The authors succeeded in obtaining analytical solutions that allowed them to describe important features such as wave focusing. The initial value problem was treated using linear non-dispersive and linear dispersive theories (analytically) and nonlinear non-dispersive and weakly nonlinear weakly dispersive theories (numerically).

The 2+1D problem was numerically investigated by Ren et al. (2019). They tested sources with kinematic variables for the 2004 Sumatra-Andaman and 2011 Tohoku earthquakes, and a worst-case scenario (Mw 9.3 earthquake) in the Manila trench. This study showed that significant improvements in matching the tsunami arrival times and amplification of the waves are achieved when slow ruptures are considered. The slowest velocity rupture tested was 1.0 km/s, where major differences were noted in comparison with the static case.

With regard to slow earthquakes, tsunami earthquakes are a special case (Polet and Kanamori 2009), generally with rupture velocities slower (~ 1 km/s) than with regular earthquakes ($\sim 2.0 - 2.7$ km/s). Nonetheless, rare extreme cases have been observed. Bell et al. (2014) reevaluated the 1947 Offshore Poverty Bay tsunami earthquake, obtaining unusual rupture velocities $(0.15 - 0.30)$ km/s. These types of earthquakes are especially important because they can excite dangerous tsunami waves with almost no shaking, and are thus unnoticed by the local population.

This work explores the effects of kinematic parameters of the seismic source on tsunami wave propagation through analytical solutions in the wavenumber domain. We extend the previous studies to consider arbitrary bilateral ruptures, and an explicit solution in time is derived for the non-dispersive case and the amplification factor is obtained in exact form.

In Sect. 2, the mathematical model and assumptions are explained. Section 3 describes the derivation of the analytical solutions. Numerical experiments and results are given in Sect. 4. Finally, a discussion and conclusion are presented in Sect. 5.

Details on the mathematical derivations are given in Appendices A and B.

2. Mathematical Model

One of the simplest models regarding analytical tsunami solutions is a flat infinite ocean with a fixed depth of h. To account for timescales attributed to underwater perturbations, an active generation should be formulated (Fig 1).

The potential tsunami theory has been widely studied in this setup (Hammack 1973; Kervella et al. 2007; Dutykh and Dias 2007; Nosov and Kolesov 2011, among others), and is adopted in this study.

2.1. Linear Potential Tsunami

For an irrotational flow, the velocity field $\mathbf{u}(x,y,z,t)$ comes from the gradient of a scalar function $\varphi(x,y,z,t)$. The nonlinear shallow water system (NSWS), in an inviscid and constant density medium, can then be expressed as

$$\begin{aligned}
&\Delta\varphi = 0\\
&\varphi_z = \zeta_t + \nabla\varphi\cdot\nabla(-h+\zeta), \text{at } z = -h+\zeta\\
&\varphi_z = \eta_t + \nabla\varphi\cdot\nabla\eta, \text{at } z = \eta\\
&\varphi_t = -\frac{1}{2}|\nabla\varphi|^2 - g\eta, \text{at } z = \eta,
\end{aligned}$$

where g is the gravity acceleration. When nonlinear effects are neglected, the NSWS is reduced to its linearized form

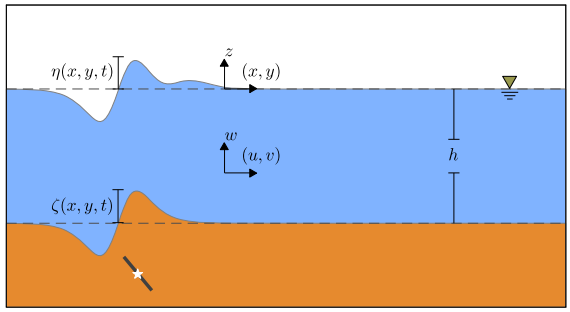

Figure 1
Geometry setup and definition of variables

$$\begin{aligned}
&\Delta\varphi = 0\\
&\varphi_z = \zeta_t, \text{at } z = -h\\
&\varphi_z = \eta_t, \text{at } z = 0\\
&\varphi_t = -g\eta, \text{at } z = 0.
\end{aligned} \tag{1}$$

The system (1) is solved by employing the Fourier transform in space and the Laplace transform in time:

$$\mathcal{F}\{f\}(\mathbf{k}) = \hat{f}(\mathbf{k}) = \int_{\mathbb{R}^N} f(\mathbf{r})e^{i\mathbf{k}\cdot\mathbf{r}}dr$$

$$\mathcal{L}\{g\}(s) = \overline{f}(s) = \int_{0^-}^{\infty} g(t)e^{-st}dt$$

which gives

$$\begin{aligned}
&\overline{\widehat{\varphi}}(k_x,k_y,z,s) = -\frac{g}{\cosh(kh)(s^2+\omega^2)}\\
&\cdot\left\{\left(s\overline{\widehat{\zeta}}(k_x,k_y,s) - \widehat{\zeta}(k_x,k_y,0^-)\right)\right.\\
&\left.\left[\cosh(kz) - \frac{s^2}{gk}\sinh(kz)\right] + \cosh(k(z+h))\widehat{\eta_0}(k_x,k_y)\right\},
\end{aligned}$$

and, in particular, the surface elevation can be retrieved in terms of the underwater disturbance

$$\begin{aligned}
&\overline{\widehat{\eta}}(k_x,k_y,s) = \frac{s}{s^2+\omega^2}\\
&\left\{\frac{s\overline{\widehat{\zeta}}(k_x,k_y,s) - \widehat{\zeta}(k_x,k_y,0^-)}{\cosh(kh)} + \widehat{\eta_0}(k_x,k_y)\right\}
\end{aligned} \tag{2}$$

where $\omega^2 = (ck)^2\frac{\tanh(kh)}{kh}$, $k^2 = k_x^2 + k_y^2$, $c = \sqrt{gh}$ and $\eta_0(x,y)$ is the initial condition. In this work, $\eta_0(x,y)$ is set to zero.

2.2. The Underwater Disturbance

The term $\zeta(x,y,t)$ is modeled following the main features of dip-slip earthquakes and is linked to a fault with dip angle δ buried just under the disturbance and breaks from the ocean bottom to its width W (see Fig. 2). The idea is to choose a function that allows one to explicitly invert the Laplace transform. Here, we propose an uncoupled function in (x, y), i.e., $\zeta(x,y,t) = \zeta_0^x(x)\zeta_0^y(y)T(y,t)$, where T models a simple time source function that is called when the rupture front reaches (x, y) and makes ζ linearly pass from zero to its final value in a time interval of t_R (the rise time). Because spatial complexity along the strike direction is neglected, $\zeta_0^y(y)$ is constant and can

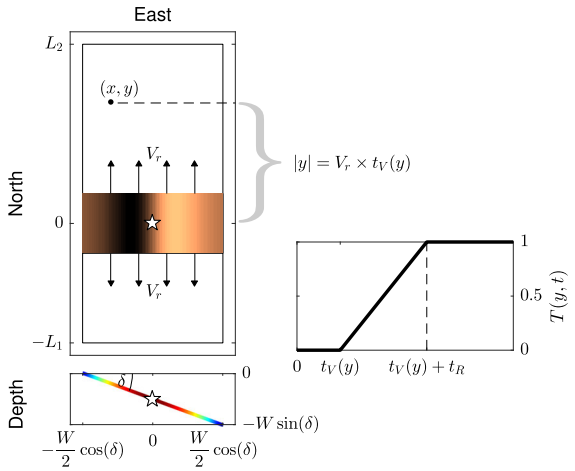

Figure 2
Sketch of the underwater forcing term. The color scale in the lower panel illustrates the heterogeneity of the fault slip

be set simply as $\zeta_0^y(y) = \mathcal{H}([L_2 - y][y + L_1])$, where $\mathcal{H}(\cdot)$ denotes the Heaviside step function and $L =: L_1 + L_2$ is the total fault length. This assumption is mainly taken to facilitate the derivation of analytical solutions, but also allows us to isolate possible interactions between the rupture front that moves at constant speed V_R and slip complexity on the source. The rupture front is modeled as a plane front that propagates along the strike direction at constant speed. The reason for making the advance dependent only on the strike direction is, first, to simplify the derivation of the analytical solution, and second, because of the fault dimension scales. Hereafter, we will work with the apparent rupture velocity $V_r =: V_R \cos(\delta)$.

Along the dip direction, the disturbance is modeled as a classical N-wave (Tadepalli and Synolakis 1994):

$$\zeta_0^x(x) = -\frac{3\sqrt{3}}{2} H \operatorname{sech}^2(\gamma x)\tanh(\gamma x)$$

where $\gamma = \frac{1}{W\cos(\delta)}\operatorname{arcsech}(\sqrt{1-r})$ and r is the surface percentage of the N-wave that lies over the projection of the fault in $z = 0$. This value is set as $r = 0.999$. γ is constrained this way to ensure that the fault does not produce a deformation far from the source area.

This N-wave has an explicit Fourier transform:

$$\widehat{\zeta_0^x}(k_x) = \frac{3\sqrt{3}\pi}{4} H\gamma^3 \operatorname{csch}(\alpha k_x) k_x^2 i$$

with $\alpha = \frac{\pi}{2\gamma}$.

To set the fault parameters, the scaling laws from Blaser et al. (2010) are chosen

$$\log(W) = -1.86 + 0.46 M_w$$
$$\log(L) = -2.37 + 0.57 M_w$$

Usually, the bottom disturbance is obtained from a slip distribution, but in this case, we impose the shape of the bottom deformation for analytical convenience. This means that H has to be constrained to produce the target moment magnitude. To perform this task, first, it should be noted that H is linear in $\eta_0^x(x)$. Second, we call $D(s)$ the slip distribution profile along the dip, then

$$\zeta_0^x(x) = \int_0^W K(x, s) D'(s) ds,$$

where $K(x, s)$ is the kernel derived by Freund and Barnett (1976) and later corrected by Madariaga (2003). With this, $D(s)$ is inverted by discretizing the integral and employing the L-curve method for a non-negative least square problem (NNLS) with a Tikhonov regularization of smoothness (Hansen 1994). This is solved for $H = 1$, and then scaled to the desired seismic moment $M_0 = \mu L \int_0^W D(s) ds$, for a given shear modulus μ.

Finally, the source time function used is

$$T(y, t) = S\left(\frac{t - t_V}{t_R}\right),$$

where $S(x) = x\mathcal{H}(x) - (x-1)\mathcal{H}(x-1)$. In other words, the source time rate function at each point is a boxcar that starts at the rupture time t_V and the last rise time t_R.

3. Analytical Solution

3.1. 2+1D Dispersive Solution

A detailed derivation is presented in the appendix. Using the source time function shown in Fig. 2, with $t_V = \frac{|y|}{V_r}$ from Eq. (3), the analytical solution found, in the wavenumber domain, is

$$\widehat{\eta}(k_x,k_y,t)=\frac{\widehat{\zeta_0^x}(k_x)}{\cosh(kh)}\frac{V_r^2}{t_R}[\phi(t)-\phi(t-t_R)] \quad (3)$$

where

$$\begin{aligned}\phi(t)=&\frac{2}{V_r}p(t,0)-\frac{1}{V_r}\cos(L_2k_y)p(t,t_2)+k_y\sin(L_2k_y)q(t-t_2)\\&-\frac{1}{V_r}\cos(L_1k_y)p(t,t_1)+k_y\sin(L_1k_y)q(t-t_1)\\&+i\left\{-\frac{1}{V_r}\sin(L_2k_y)p(t,t_2)-k_y\cos(L_2k_y)q(t-t_2)\right.\\&\left.+\frac{1}{V_r}\sin(L_1k_y)p(t,t_1)+k_y\cos(L_1k_y)q(t-t_1)\right\}\end{aligned}$$

and $t_i=\frac{L_i}{V_r}$. Functions p and q are defined in Appendix A. Equation (3) is numerically inverted with a fast Fourier transform.

A similar solution was derived by Ward (2001) to model a submarine landslide.

3.2. 1+1D Non-Dispersive Solution

To obtain a closed analytical solution, the non-dispersive case is used. In this case, to retrieve a 1+1D solution it is sufficient to replace $\eta_0^x(x)=H$ in Eq. (2), and for long waves, $\omega\approx ck$ is assumed (non-dispersive).

To simplify the analysis, only a unilateral propagation is considered with a null rise time ($t_R=0$). Therefore, the analytical solution is

$$\begin{aligned}\eta(y,t)=&\frac{\nu^2H}{\pi(1-\nu^2)}\\&\left[\psi(y-V_rt,0)+\psi(ct-y,0)+\left(\frac{1}{\nu}-1\right)\psi(ct,y)\right.\\&+\mathcal{H}(t')\left\{\psi(L+V_rt'-y,0)-\frac{1}{2}\left(\frac{1}{\nu}-1\right)\psi(y-L+ct',0)\right.\\&\left.\left.+\frac{1}{2}\left(\frac{1}{\nu}+1\right)\psi(y-L-ct',0)\right\}\right]\end{aligned} \quad (4)$$

where ν is the ratio between velocities, $\frac{V_r}{c}$, $t'=t-\frac{L}{V_r}$, and $\psi(x,y)=\arctan\left(\frac{\sinh\left(\frac{\pi x}{2h}\right)}{\cosh\left(\frac{\pi y}{2h}\right)}\right)$.

3.3. The Radial Case

In the particular case when the underwater deformation is radially symmetric, the set (1) can be solved in cylindrical coordinates with the routine Hankel–Laplace transform. The solution expressed as iterated integrals is

$$\begin{aligned}\eta(r,t)=&\int_0^\infty\frac{J_0(kr)k}{\omega(k)\cosh(kh)}\int_0^\infty J_0(k\xi)\xi\\&\int_0^t\zeta_{tt}(\xi,\tau)\sin[\omega(k)(t-\tau)]d\tau d\xi dk.\end{aligned} \quad (5)$$

Equation (5) is similar to that obtained by Tuck and Hwang (1972) in a sloping beach setup except for the filter $1/\cosh(kh)$ and the frequency dispersion $\omega(k)$.

Following a similar derivation as Fuentes et al. (2018), except that now we use the standard form of the zero-order Hankel transform, and taking $t_V=\frac{r}{V_r}$ in the source time function, the solution reduces to

$$\eta(r,t)=\frac{\mathcal{M}(r,t)-\mathcal{M}(r,t-t_R)}{t_R} \quad (6)$$

with

$$\begin{aligned}\mathcal{M}(r,t)=&\int_0^\infty\frac{J_0(kr)k}{\omega(k)\cosh(kh)}\int_0^{\max(V_rt,0)}\\&J_0(k\xi)\xi\zeta_0(\xi)\sin[\omega(k)(t-\xi/V_r)]d\xi dk.\end{aligned} \quad (7)$$

$\mathcal{M}$ can be efficiently computed with minor modifications of the method of Baddour and Chouinard (2017).

4. Results

Numerical experiments show that amplification is stronger when $V_r=c$. This is in agreement with previous studies (Novikova and Ostrovsky 1979; Todorovska and Trifunac 2001; Le Gal et al. 2017; Fuentes et al. 2018). Figure 3 illustrates different wave fields associated with different rupture velocities taken from Ren et al. (2019) for comparison purposes. The example shows a unilateral rupture, where very low rupture velocities do not excite tsunami waves, whereas low velocities (around c) optimize the enhancement of the tsunami waves. The extreme case of high rupture velocity matches the classical static approach, in which the seabed deformation is copied as the initial condition in the water surface. Besides amplification phenomena, arrival times are also evidently affected. The radiation

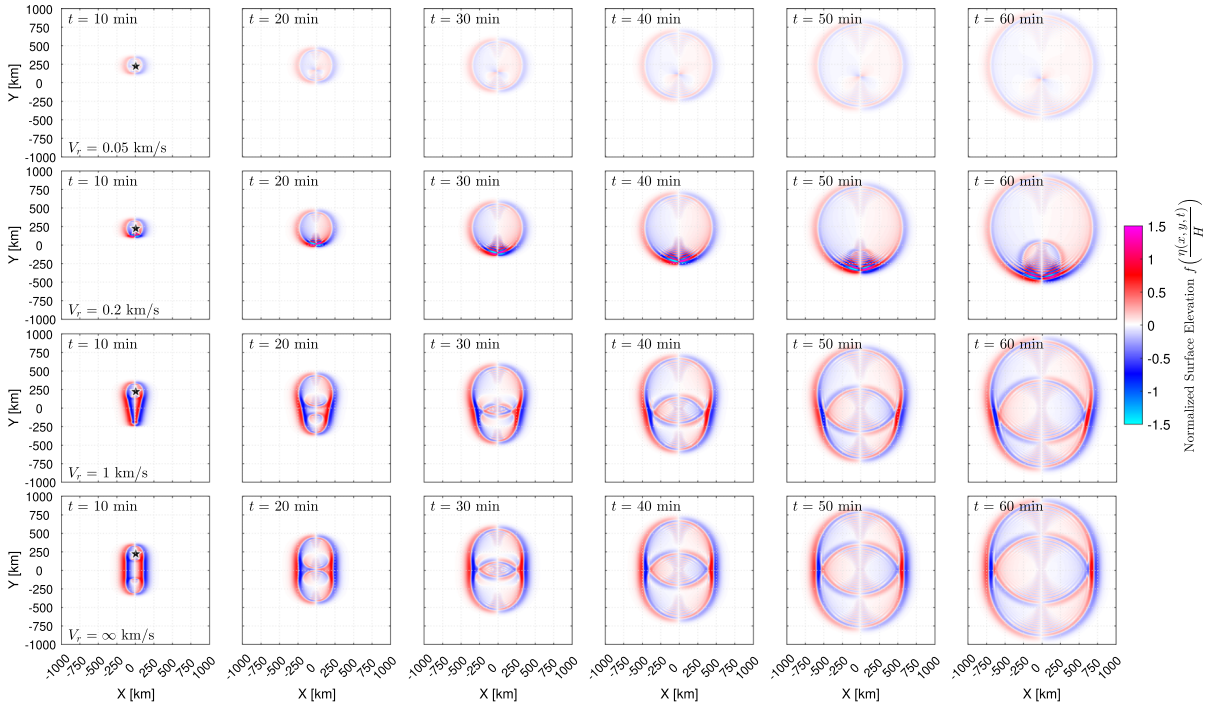

Figure 3
Snapshots of tsunami propagation for a M_w 8.8 earthquake with unilateral rupture propagation at different velocities. The source parameters are $L = 443$ km, $W = 154$ km, $\delta = 18°$, $\mu = 30$ GPa and average slip $\overline{D} = 2.2$ m. Due to the large disparity in the amplification values for different cases, the color palette is scaled with the function $f(x) = \text{sign}(x)\sqrt{|x|}$

pattern is now dependent on the rupture directivity. According to our coordinate system, for north–south ruptures (Fig. 2), stations with negative azimuths will be more delayed in their arrival times relative to the static case, which is the fastest. The opposite result is observed if the rupture propagates south–north. In a bilateral rupture, all the records will be delayed on the proportion of the rupture segmentation. This is illustrated in Figs. 6a, 7a and 8a, where a larger station symbol indicates shorter arrival time.

The wave dispersion also plays a key role in the amplification process which separates faster waves depending on their wavelengths. This is illustrated in Fig. 4 in the 1+1D case. Dispersion can diminish the amplitudes due to wave spreading, because the global energy remains the same. The closer to the critical case ($V_r = c$), the greater the amplification, with maximum reached when there are no dispersion effects. Also, if this travel lasts longer for long waves ($L/h >> 1$), then the amplification should be higher (Fig. 5). Note that the analytical solution is explicit and retrieves exact values for the non-dispersive case.

Three different experiments are considered: (A) an asymmetric bilateral rupture (Fig. 6), (B) a symmetric bilateral rupture (Fig. 7) and (C) a unilateral rupture (Fig. 8). The experiments confirm that amplification is largest at the end of the longest segment of the fault and always at the critical kinematic values: $v = 1$ and $t_R = 0$ (Table 1). The stations with higher amplification are located ahead of the rupture front, where coupling due to directivity effects are stronger. The panels (c–h) in Figs. 6, 7, 8 display the amplification at selected stations, similar to the way it was presented in Fuentes et al. (2018).

The radial case shows the importance of the rupture directivity, i.e., when the rupture front has no preferred direction but is still accounted for. Figure 9 illustrates the tsunami amplification due to slow ruptures with radial symmetry. As expected, augmentation is present, but it is much weaker than a directive case.

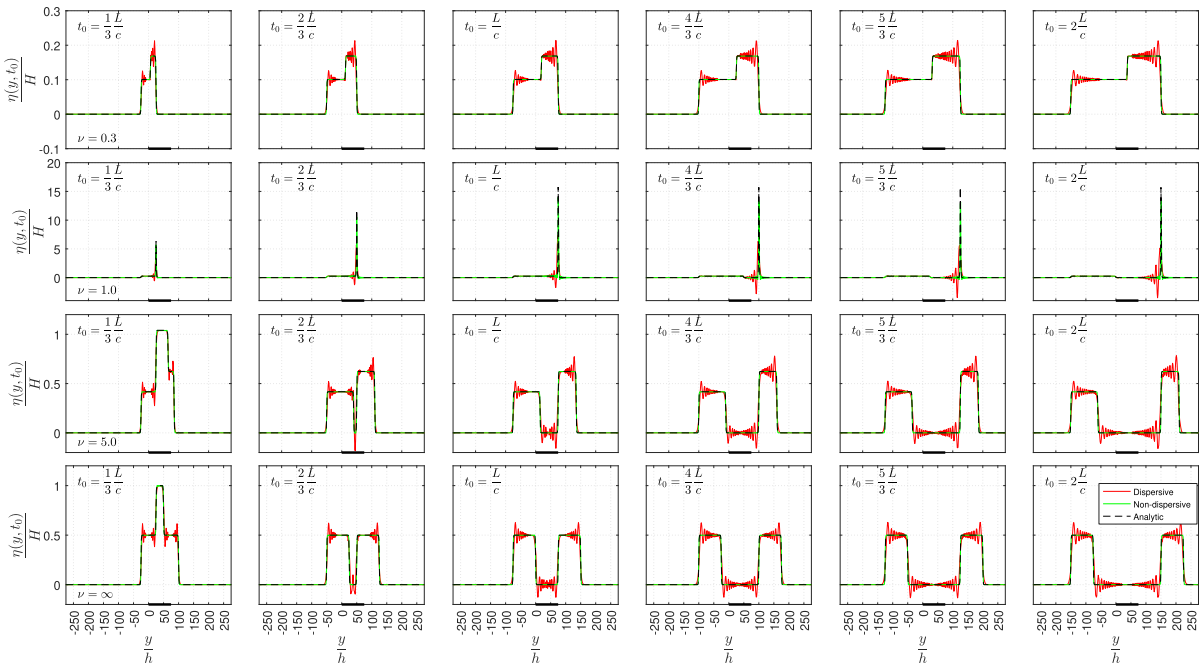

Figure 4
Snapshots at different times for different rupture velocities. The thick black line represents the fault length $L = 300$ km. All cases were computed with $h = 4$ km. Each panel shows the dispersive (Eq. 3), non-dispersive (Eq. 3 with $\omega = ck$) and analytical solutions (Eq. 4). The dispersive and non-dispersive cases correspond to a transect along $x = 0$ of the 2D domain

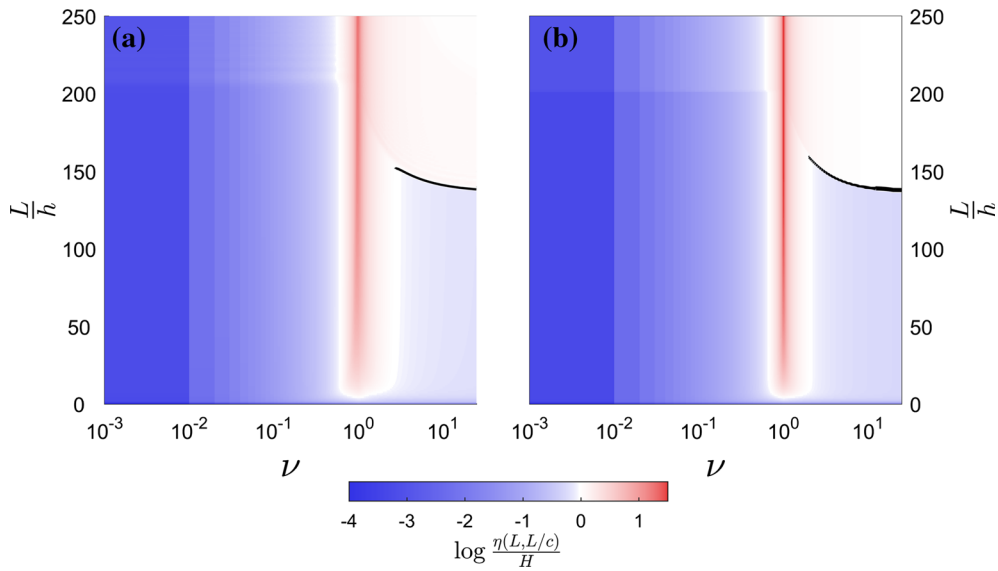

Figure 5
Color map of the maximum amplification as a function of v and $\frac{L}{h}$. **a** Dispersive solution. **b** Non-dispersive solution. The black curve indicates the level curve 0 (no amplification)

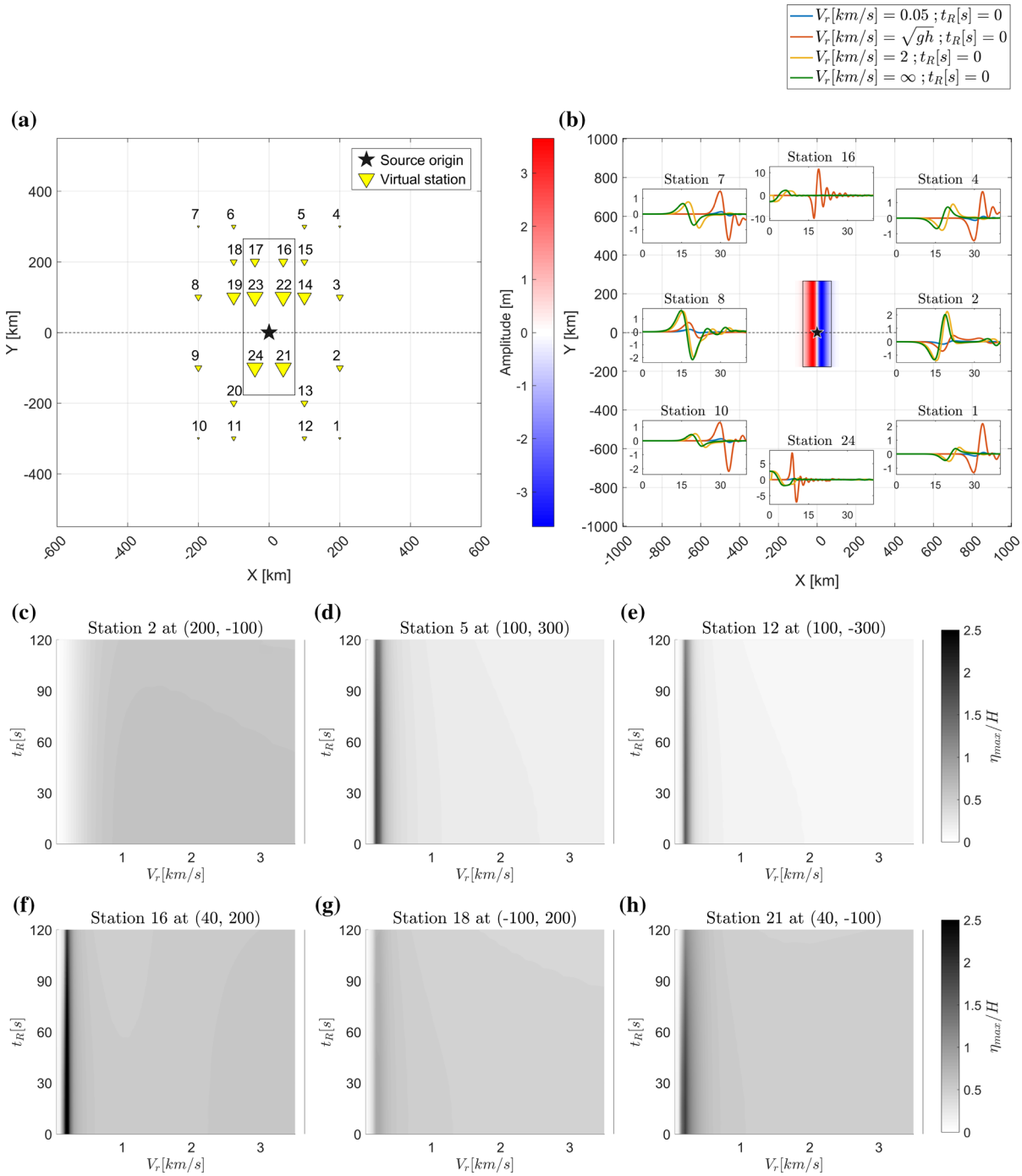

Figure 6
Asymmetric rupture propagation. **a** Network of synthetic stations. The black star represents the hypocenter. The stations are drawn with different sizes according to their arrival times. The shorter the arrival time is in the station, the larger the symbol is drawn. **b** Static initial condition. Inner panels depict the time series of given stations for different values of rupture velocity and rise time. **c–h** Maximum amplification of a given station as a function of rupture velocity and rise time

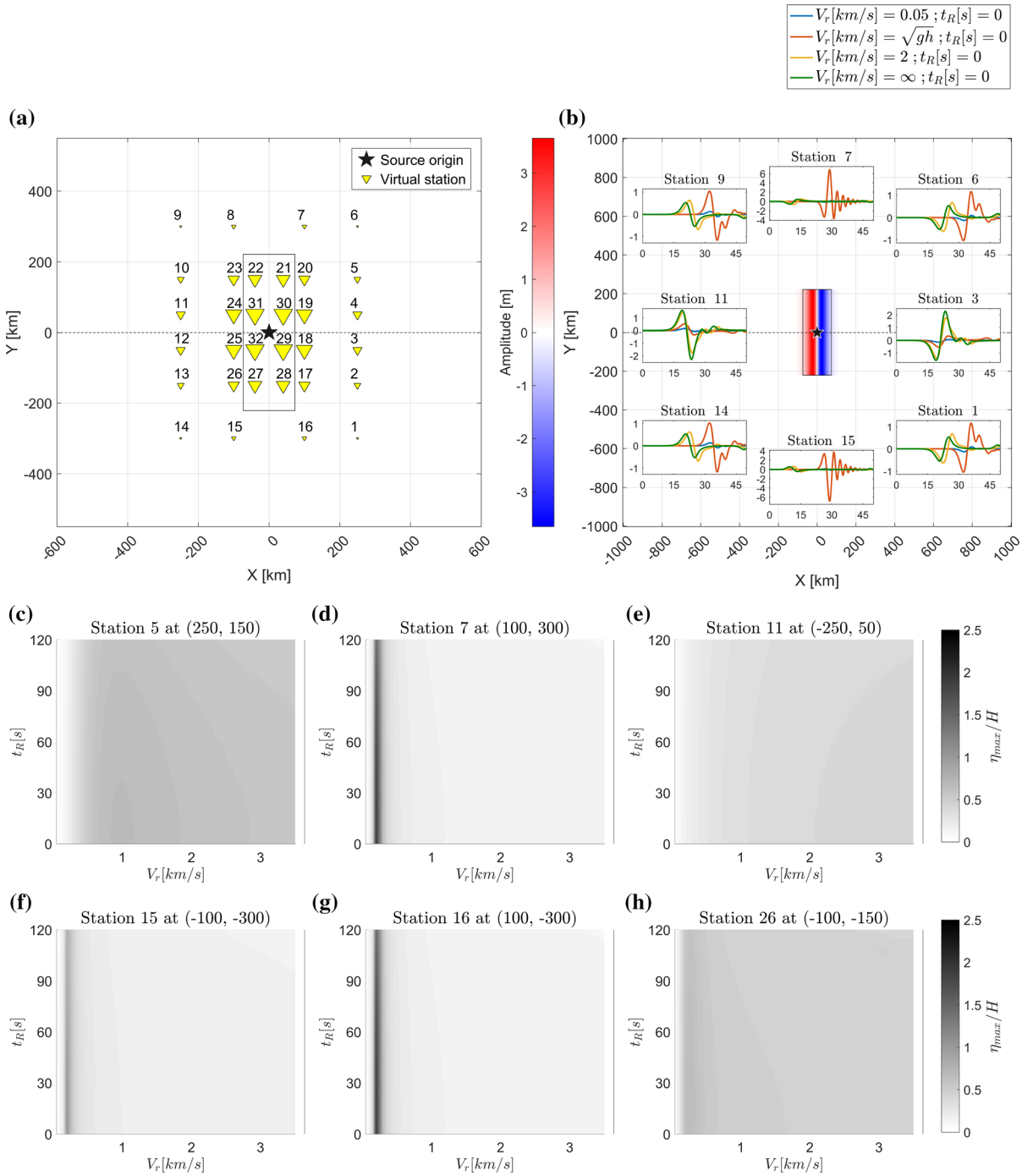

Figure 7

Symmetric rupture propagation. **a** Network of synthetic stations. The black star represents the hypocenter. The stations are drawn with different sizes according to their arrival times. The shorter the arrival time is in the station, the larger the symbol is drawn. **b** Static initial condition. Inner panels depict the time series of given stations for different values of rupture velocity and rise time. **c–h** Maximum amplification of a given station as a function of rupture velocity and rise time

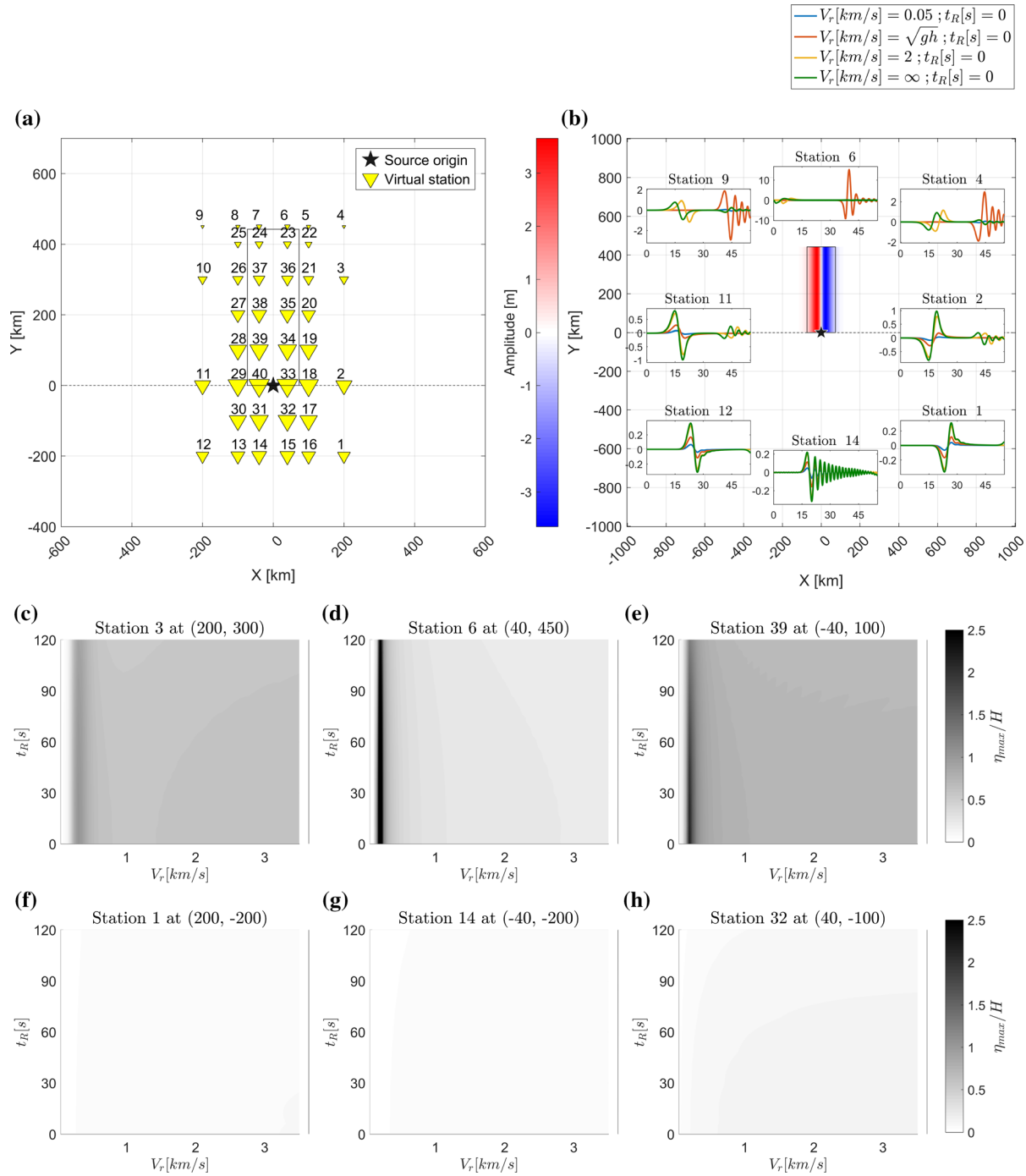

Figure 8

Unilateral rupture propagation. **a** Network of synthetic stations. The black star represents the hypocenter. The stations are drawn with different sizes according to their arrival times. The shorter the arrival time is in the station, the larger the symbol is drawn. **b** Static initial condition. Inner panels depict the time series of given stations for different values of rupture velocity and rise time. **c–h** Maximum amplification of a given station as a function of rupture velocity and rise time

Table 1

Maximum amplification recorded in each experiment

Experiment	$\frac{\eta_{max}}{H}$	Station	Location (km, km)	v	t_R
A	3.14	16	(40, 200)	1	0
B	2.70	21	(40, 150)	1	0
C	4.16	6	(40, 450)	1	0

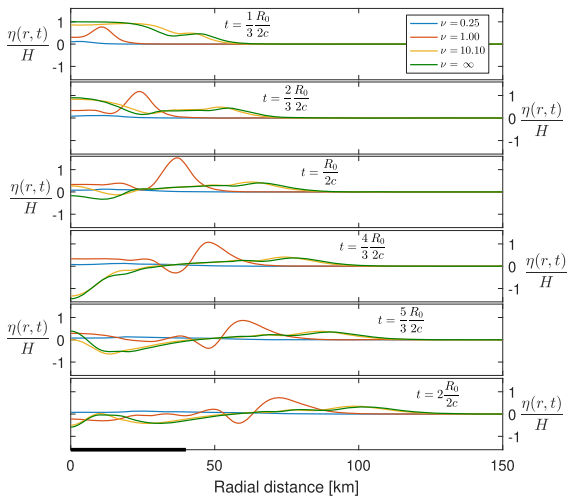

Figure 9
Propagation for different rupture velocities at different times for a radially symmetric source $\zeta_0(r) = H\mathcal{H}(R_0 - r)$

5. Discussion and Conclusions

In this work, the role of source kinematic parameters in wave tsunami development was analyzed. Those parameters are let free and independent in order to obtain the most general solution possible, regardless of whether such earthquakes can really exist. Certainly, complex situations can arise from the intrinsic nonlinearity of the earthquake dynamics and rheology (Schmedes et al. 2010; Ma 2012).

Similar solutions to Eq. (3) were used in the framework of tsunami-landslides. However, the validity of that type of application might be questionable, since the source time function used does not represent a horizontal moving slide but a vertical uplift. An example of sliding slumps was addressed by Okal and Synolakis (2003). The source time function for an underwater slide as presented in Ward (2001) should be of the form

$$\zeta(x, y, t) = H\chi_{[0,L]}(x - V_r t)\chi_{\left[-\frac{W}{2},\frac{W}{2}\right]}(y)\chi_{[0,T_s]}(t),$$

which has the following analytical solution in the (k_x, k_y) space:

$$\hat{\eta}(k_x, k_y, t) = F(k_x, k_y)\left[u(k_x, k_y, t) - e^{ik_x V_r T_s} u(k_x, k_y, t - T_s)\right]$$

where

- $\chi_{[a,b]}(x) = \mathcal{H}(x - a) - \mathcal{H}(x - b)$
- $F(k_x, k_y) = V_0 \dfrac{\mathrm{sinc}(X(k_x))\mathrm{sinc}\left(Y(k_y)\right)}{\cosh(kh)} e^{ik_x \frac{L}{2}} \mathcal{H}(T_s)$
- $V_0 = LWH$ is the total volume of the sliding body
- $X(k_x) = \dfrac{k_x L}{2}$ and $Y(k_y) = \dfrac{k_y W}{2}$
- $u(k_x, k_y, t) = \cos(\omega t)\mathcal{H}(t) + \dfrac{ik_x V_r}{\omega^2 - (k_x V_r)^2}$
  $\left[\omega \sin(\omega t) - ik_x V_r \cos(\omega t) + ik_x V_r e^{ik_x V_r t}\right]\mathcal{H}(t)$
- and T_s is the slide duration. $T_s = +\infty$ if $V_r = 0$.

This solution has nonphysical $\cos(\omega t)$ terms associated with the jump discontinuities of the source time function due to its abrupt start and braking. A better modeling requires one to account for the acceleration of the slide, as was noted by Okal and Synolakis (2003). The study of tsunami landslide sources is outside the scope of this work, and they will be reviewed in a dedicated survey.

The kinematics of the tsunamigenic source process can strongly influence the waveforms, especially in the near field, close to the source area. The main reason is due to the coupling between the rupture front and the velocity of tsunami waves. When this coupling becomes stronger, at every time t, waves are generated in phase, creating constructive interference. This process is depicted in Fig. 10. When a tsunami wave is created by an underwater uplift, it starts to travel radially. The red dashed curve represents the waveform after a given time interval dt. However, at that time a new wave is generated, shown in the dashed black line. Both curves contribute to the final waveform, and this process repeats continuously during the rupture duration (see the supplemental material). This effect counteracts with the dispersion, which diminishes the wave amplitudes. When there is no dispersion, from Eq. (4) it can be inferred that the maximum amplification occurs in the critical case $(v, t_R) = (1, 0)$ at the endpoint of the largest segment:

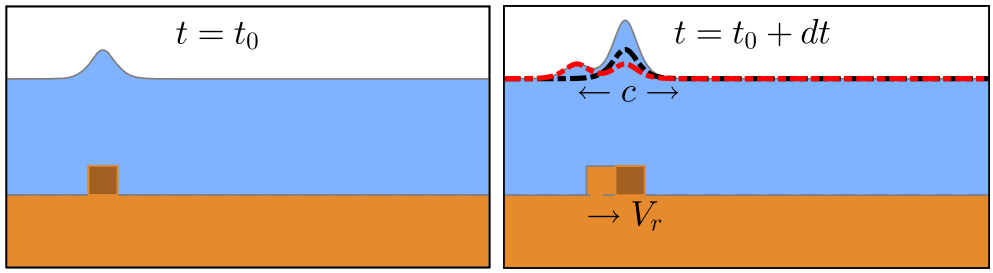

Figure 10
Sketch of the amplification process

$$\lim_{V_r \to c} \frac{\eta\left(L_0, \frac{L_0}{c}\right)}{H} = \frac{L_0}{4h} + \frac{1}{8},$$

with $L_0 = \max\{L_1, L_2\}$. This can be seen as an upper bound, but should be expected in cases where dispersion is not present, for instance, in solitary waves. This result shows that the peak amplitude is optimal for unilateral ruptures, since there is a longer distance where the constructive interference process takes place and grows in proportion to the fault length.

Even for accepted values of rupture velocity (1.5–2.0 km/s), Williamson et al. (2019) found non-negligible delays in arrival times, which is in agreement with our results. The authors did not observe significant amplifications, but the reason is because they worked with ratio of velocities v of 7.5 to 10. Nevertheless, amplification becomes important for lower values of v: 2.0 and 2.7 for the dispersive and non-dispersive cases, respectively (Fig. 5). For $v < 0.1$, there is no amplification, because in this region tsunami waves are not excited.

Acknowledgements

This work was supported in part by the *Programa de Riesgo Sísmico* and FONDECYT grant 1170218.

Appendix 1: Detailed Mathematical Derivation

2+1D Case

In the following, detailed derivations are shown step by step. The classical solution for the irrotational long-wave tsunami approach in a constant ocean depth is

$$\overline{\overline{\eta}}(k_x, k_y, s) = \frac{s^2}{s^2 + \omega^2} \frac{\overline{\overline{\zeta}}(k_x, k_y, s)}{\cosh(kh)} \tag{8}$$

where $\omega^2 = gk\tanh(kh)$, $k^2 = k_x^2 + k_y^2$, g is the gravity acceleration and h is the ocean depth. The seafloor displacement is modeled as

$$\zeta(x, y, t) = \zeta_0^x(x)\zeta_0^y(y)T(y, t) \tag{9}$$

with

$$T(y, t) = S\left(\frac{t - t_V(y)}{t_R}\right), \tag{10}$$

with the function $S(x) = x\mathcal{H}(x(1-x)) + \mathcal{H}(x-1)$.

Firstly, we compute the Fourier–Laplace transform of T. Note that

$$\mathcal{L}\{S\}(s) = \frac{1}{s^2}(1 - e^{-s}). \tag{11}$$

Then, by the Laplace transform properties of time shift and scaling, we obtain

$$\begin{aligned} \mathcal{L}\{T\}(s) &= t_R\,\overline{S}(t_R s)e^{-t_V(y)s} \\ &= \frac{1}{t_R s^2}(1 - e^{-st_R})e^{-t_V(y)s}. \end{aligned} \tag{12}$$

Now we need to compute the following Fourier transform:

$$\mathcal{F}\left\{\zeta_0^y(y)e^{-t_V(y)s}\right\}(k_y), \tag{13}$$

which depends on the rupture model. In this case, a general bidirectional propagation is chosen.

The origin of the coordinate system is set at the starting rupture point. The rectangular fault is then divided into two parts, one segment to the north of length L_2 and one segment to the south of length L_1, accounting for the total length $L = L_1 + L_2$. Thus,

$\zeta_0^y(y) = \mathcal{H}((L_2 - y)(y + L_1))$ and $t_V(y) = \frac{|y|}{V_r}$. Computation of expression (13) results in

$$\begin{aligned}\mathcal{F}\left\{\zeta_0^y(y)e^{-t_V(y)s}\right\}(k_y) &= \int_{-L_1}^{L_2} e^{-\frac{s}{V_r}|y|+ik_y y}dy \\ &= \int_{-L_1}^{0} e^{\frac{s}{V_r}y+ik_y y}dy + \int_{0}^{L_2} e^{-\frac{s}{V_r}y+ik_y y}dy \\ &= F\left(\frac{s}{V_r}, k_y, 0\right) - F\left(\frac{s}{V_r}, k_y, -L_1\right) \\ &\quad + F\left(-\frac{s}{V_r}, k_y, L_2\right) - F\left(-\frac{s}{V_r}, k_y, 0\right)\end{aligned}$$

where $F(a,b,x) = \frac{e^{ax}}{a^2+b^2}\left[\left(a\cos(bx) + b\sin(bx)\right) + i\left(a\sin(bx) - b\cos(bx)\right)\right]$.

Inserting in Eq. 8,

$$\begin{aligned}\overline{\widehat{\eta}}(k_x, k_y, s) = &\frac{\widehat{\zeta_0^x}(k_x)}{\cosh(kh)}\frac{V_r^2}{t_R}(1 - e^{-t_R s})\frac{1}{s^2 + \omega^2} \\ &\times \frac{1}{s^2 + (k_y V_r)^2} \\ &\left[\frac{2}{V_r}s + e^{-\frac{L_2}{V_r}s}\left\{-\frac{s}{V_r}\cos(L_2k_y) + k_y\sin(L_2k_y)\right\}\right. \\ &- e^{-\frac{L_1}{V_r}s}\left\{\frac{s}{V_r}\cos(L_1k_y) - k_y\sin(L_1k_y)\right\} \\ &+ ie^{-\frac{L_2}{V_r}s}\left\{-\frac{s}{V_r}\sin(L_2k_y) - k_y\cos(L_2k_y)\right\} \\ &\left.+ie^{-\frac{L_1}{V_r}s}\left\{\frac{s}{V_r}\sin(L_1k_y) + k_y\cos(L_1k_y)\right\}\right]\end{aligned} \tag{14}$$

Since $\mathcal{L}\{\sin(at)\mathcal{H}(t)\}(s) = \frac{a}{s^2+a^2}$, we can define $q(a,b,t) =: \frac{\mathcal{H}(t)}{a^2-b^2}\left(\frac{\sin(bt)}{b} - \frac{\sin(at)}{a}\right)$, and then we have that $\overline{q}(a,b,s) = \frac{1}{s^2+a^2}\cdot\frac{1}{s^2+b^2}$, with $a = \omega$ and $b = k_y V_r$.

Defining $p(a,b,t,t_0) =: \mathcal{L}^{-1}\{se^{-st_0}\overline{q}(a,b,s)\}(t) = \partial_t q(a,b,t-t_0)$ and using the properties of the Laplace transform, Eq. 15 can be rewritten in terms of q and p (function arguments are omitted for the sake of simplicity)

$$\widehat{\eta}(k_x, k_y, t) = \frac{\widehat{\zeta_0^x}(k_x)}{\cosh(kh)}\frac{V_r^2}{t_R}[\phi(t) - \phi(t - t_R)] \tag{15}$$

where

$$\begin{aligned}\phi(t) = &\frac{2}{V_r}p(t,0) - \frac{1}{V_r}\cos(L_2k_y)p(t,t_2) + k_y\sin(L_2k_y)q(t-t_2) \\ &- \frac{1}{V_r}\cos(L_1k_y)p(t,t_1) + k_y\sin(L_1k_y)q(t-t_1) \\ &+ i\left\{-\frac{1}{V_r}\sin(L_2k_y)p(t,t_2) - k_y\cos(L_2k_y)q(t-t_2)\right. \\ &\left.+\frac{1}{V_r}\sin(L_1k_y)p(t,t_1) + k_y\cos(L_1k_y)q(t-t_1)\right\}\end{aligned} \tag{16}$$

and $t_i = \frac{L_i}{V_r}$, $i \in \{1,2\}$. Note that there are removable singularities in functions p and q when $\omega = V_r k_y$.

The static deformation can be retrieved by letting $V_r \to \infty$ and $t_R \to 0$, which gives

$$\begin{aligned}\widehat{\eta}(k_x, k_y, t) = &\frac{\widehat{\zeta_0^x}(k_x)}{k_y\cosh(kh)} \\ &\left[\sin(k_yL_2) + \sin(k_yL_1) + i\{\cos(k_yL_1) - \cos(k_yL_2)\}\right] \\ &\cos(\omega t).\end{aligned} \tag{17}$$

Observe that the symmetric bilateral case has no frequency shifts and leads to a pure real spectrum

$$\widehat{\eta}(k_x, k_y, t) = L\frac{\widehat{\zeta_0^x}(k_x)}{\cosh(kh)}\operatorname{sinc}\left(\frac{k_yL}{2}\right)\cos(\omega t). \tag{18}$$

Finally, the water surface is inverted with a fast Fourier transform (FFT) algorithm:

$$\eta(x, y, t) = \mathcal{F}^{-1}\left\{\widehat{\eta}(k_x, k_y, t)\right\}(x, y).$$

1+1D Case

If 2D effects are neglected, $\zeta_0^x(x) = H$ and $\widehat{\zeta_0^x}(k_x) = 2\pi\delta(k_x)$. Equation (16) then becomes

$$\widehat{\eta}(k_y, t) = \frac{H}{\cosh(k_yh)}\frac{V_r^2}{t_R}[\phi(t) - \phi(t - t_R)]. \tag{19}$$

Again, the final solution $\eta(y,t)$ can be retrieved from Eq. (20) with the 1D FFT.

In order to better understand analytically the behavior of the amplification as a function of rupture velocity, only a unidirectional rupture is treated with a instant rise time, that is to say, $L_1 = 0, L_2 = L$ and $t_R = 0$. Equation (20) becomes

$$\widehat{\eta}(k_y, t) = \frac{H}{\cosh(k_yh)}V_r^2\phi'(k_y, t) \tag{20}$$

with

$$\phi'(k_y,t) = \frac{1}{V_r}p'(t,0) - \frac{1}{V_r}\cos(Lk_y)p'(t,t^*) + k_y\sin(Lk_y)q'(t-t^*) + i\left\{-\frac{1}{V_r}\sin(Lk_y)p'(t,t^*) - k_y\cos(Lk_y)q'(t-t^*) + k_yq'(t)\right\} \tag{21}$$

and $t^* = L/V_r$. To make possible the derivation of an analytical solution, it is necessary to neglect the dispersive effects: $\omega(k_y) \approx ck_y$.

Performing the inverse Fourier transform term by term, by symmetry, each is of the form

$$\psi(x,y) = \int_0^\infty \frac{\sin(k_yx)\cos(k_yy)}{k_y\cosh(k_yh)}dk_y = \arctan\left(\frac{\sinh\left(\frac{\pi x}{2h}\right)}{\cosh\left(\frac{\pi y}{2h}\right)}\right). \tag{22}$$

Thus, the solution is

$$\eta(y,t) = \frac{v^2H}{\pi(1-v^2)}\left[\psi(y-V_rt,0) + \psi(ct-y,0) + \left(\frac{1}{v}-1\right)\psi(ct,y). + \mathcal{H}(t')\{\psi(L+V_rt'-y,0) - \frac{1}{2}\left(\frac{1}{v}-1\right)\psi(y-L+ct',0) + \frac{1}{2}\left(\frac{1}{v}+1\right)\psi(y-L-ct',0)\right\}\right] \tag{23}$$

where $t' = t - t^*$.

In particular, when v tends to 1 ($V_r = c$), the maximum amplification at the end of the fault is

$$\frac{\eta\left(L,\frac{L}{c}\right)}{H} = \frac{L}{4h} + \frac{1}{2\pi}\psi(L,L) \approx \frac{L}{4h} + \frac{1}{8}. \tag{24}$$

Appendix 2: Derivation of Function $\psi(x,y)$

First, for any $h > 0$, let us define the function $\varphi(x)$ as follows:

$$\varphi(x) = \int_0^\infty \frac{\sin(kx)}{k\cosh(kh)}dk. \tag{25}$$

Then,

$$\psi(x,y) = \frac{1}{2}[\varphi(x+y) - \varphi(y-x)]. \tag{26}$$

By the Leibniz rule,

$$\partial_x\varphi(x) = \int_0^\infty \frac{\cos(kx)}{\cosh(kh)}dk \tag{27}$$

The integral 28 can be easily evaluated by standard complex contour integration. For this type of integral, the contour is the rectangle defined by the corners $(R, 0)$; $\left(R, \frac{\pi i}{h}\right)$; $\left(-R, \frac{\pi i}{h}\right)$; $(-R, 0)$ enclosing a simple pole at $\frac{\pi i}{2h}$, satisfying the convergence conditions.

Therefore, by the residue theorem,

$$\partial_x\varphi(x) = \frac{\pi}{2h}\operatorname{sech}\left(\frac{\pi x}{2h}\right). \tag{28}$$

Since $\varphi(0) = 0$ and $\int \operatorname{sech}(ax)dx = \frac{1}{a}\arctan(\sinh(ax)) + C$, integration of (28) allows us to retrieve φ:

$$\varphi(x) = \arctan\left(\sinh\left(\frac{\pi x}{2h}\right)\right). \tag{29}$$

By using the property $\arctan(a) \pm \arctan(b) = \arctan\left(\frac{a\pm b}{1\mp ab}\right)$, it is equivalent to write

$$\varphi(x) = 2\arctan\left(e^{\frac{\pi x}{2h}}\right) - \frac{\pi}{2}. \tag{30}$$

. Finally, replacing in(27) and manipulating the arguments, the result holds.

Publisher's Note Springer Nature remains neutral with regard to jurisdictional claims in published maps and institutional affiliations.

References

Baddour, N., & Chouinard, U. (2017). Matlab code for the discrete Hankel transform. *Journal of Open Research Software*, *5*(1), 4.

Bell, R., Holden, C., Power, W., Wang, X., & Downes, G. (2014). Hikurangi margin tsunami earthquake generated by slow seismic rupture over a subducted seamount. *Earth and Planetary Science Letters*, *397*, 1–9.

Blaser, L., Krüger, F., Ohrnberger, M., & Scherbaum, F. (2010). Scaling relations of earthquake source parameter estimates with special focus on subduction environment. *Bulletin of the Seismological Society of America*, *100*(6), 2914–2926.

Carrier, G. F., & Yeh, H. (2005). Tsunami propagation from a finite source. *Computer Modeling in Engineering and Sciences*, *10*(2), 113–121.

Dutykh, D., & Dias, F. (2007). Water waves generated by a moving bottom. In A. Kundu (Ed.), *Tsunami and Nonlinear Waves*. Berlin: Springer.

Freund, L. B., & Barnett, D. M. (1976). A two-dimensional analysis of surface deformation due to dip-slip faulting. *Bulletin of the Seismological Society of America*, *66*(3), 667–675.

Fuentes, M., Riquelme, S., Ruiz, J., & Campos, J. (2018). Implications on 1+ 1 D Tsunami runup modeling due to time features of the earthquake source. *Pure and Applied Geophysics*, *175*(4), 1393–1404.

Hammack, J. L. (1973). A note on tsunamis: their generation and propagation in an ocean of uniform depth. *Journal of Fluid Mechanics*, *60*(4), 769–799.

Hansen, P. C. (1994). Regularization tools: a Matlab package for analysis and solution of discrete ill-posed problems. *Numerical Algorithms*, *6*(1), 1–35.

Kajiura, K. (1970). Tsunami source, energy and the directivity of wave radiation. *Bulletin of Earthquake Research Institute*, *48*, 835–869.

Kânoğlu, U., Titov, V. V., Moore, C., Stefanakis, T. S., Zhou, H., Spillane, M., et al. (2013). Focusing of long waves with finite crest over constant depth. *Proceedings of the Royal Society A*, *469*(2153), 20130015.

Kervella, Y., Dutykh, D., & Dias, F. (2007). Comparison between three-dimensional linear and nonlinear tsunami generation models. *Theoretical and Computational Fluid Dynamics*, *21*(4), 245–269.

Le Gal, M., Violeau, D., Ata, R., & Wang, X. (2018). Shallow water numerical models for the 1947 Gisborne and 2011 Tohoku-Oki tsunamis with kinematic seismic generation. *Coastal Engineering*, *139*, 1–15.

Le Gal, M., Violeau, D., & Benoit, M. (2017). Influence of time-scales on the generation of seismic tsunamis. *European Journal of Mechanics-B/Fluids*, *65*, 257–273.

Ma, S. (2012). A self-consistent mechanism for slow dynamic deformation and tsunami generation for earthquakes in the shallow subduction zone. *Geophysical Research Letters*, *39*, L11310.

Madariaga, R. (2003). Radiation from a finite reverse fault in a half space. *Pure Applied Geophysics*, *160*, 555–577.

Nosov, M. A., & Kolesov, S. V. (2011). Optimal initial conditions for simulation of seismotectonic tsunamis. *Pure and Applied Geophysics*, *168*(6–7), 1223–1237.

Novikova, L. E., & Ostrovsky, L. A. (1979). Excitation of tsunami waves by a traveling displacement of the ocean bottom. *Marine Geodesy*, *2*(4), 365–380.

Novikova, L. E., & Ostrovsky, L. A. (1982). On the acoustic mechanism of tsunami wave excitation. *Oceanology*, *22*(5), 693–697.

Okal, E. A., & Synolakis, C. E. (2003). A theoretical comparison of tsunamis from dislocations and landslides. *Pure and Applied Geophysics*, *160*(10–11), 2177–2188.

Polet, J., & Kanamori, H. (2009). Tsunami earthquakes. In R. Meyers (Ed.), *Encyclopedia of complexity and systems science*. New York: Springer.

Ren, Z., Liu, H., Zhao, X., Wang, B., & An, C. (2019). Effect of kinematic fault rupture process on tsunami propagation. *Ocean Engineering*, *181*, 43–58.

Saito, T. (2013). Dynamic tsunami generation due to sea-bottom deformation: analytical representation based on linear potential theory. *Earth, Planets and Space*, *65*(12), 1411–1423.

Schmedes, J., Archuleta, R. J., & Lavallée, D. (2010). Correlation of earthquake source parameters inferred from dynamic rupture simulations. *Journal of Geophysical Research*, *115*, B03304.

Tadepalli, S., & Synolakis, C. E. (1994). The run-up of N-waves on sloping beaches. *Proceedings of the Royal Society of London Series A*, *445*(1923), 99–112.

Todorovska, M. I., & Trifunac, M. D. (2001). Generation of tsunamis by a slowly spreading uplift of the sea floor. *Soil Dynamics and Earthquake Engineering*, *21*(2), 151–167.

Tuck, E. O., & Hwang, L. S. (1972). Long wave generation on a sloping beach. *Journal of Fluid Mechanics*, *51*(3), 449–461.

Ward, S. N. (2001). Landslide tsunami. *Journal of Geophysical Research*, *106*(B6), 11201–11215.

Williamson, A., Melgar, D., & Rim, D. (2019). The effect of earthquake kinematics on tsunami propagation. *Journal of Geophysical Research: Solid Earth*, *124*, 11639–11650.

Yamashita, T., & Sato, R. (1974). Generation of tsunami by a fault model. *Journal of Physics of the Earth*, *22*(4), 415–440.

(Received March 9, 2020, revised June 1, 2020, accepted June 2, 2020)